Forces in Mechanics 8 (2022) 100109

Contents lists available at ScienceDirect

Forces in Mechanics

journal homepage: www.sciencedirect.com/journal/forces-in-mechanics

Laser powder bed fusion of AlSi10Mg alloy: Numerical investigation on the temperature field evolution

Sara Ricci [*], Gabriel Testa, Gianluca Iannitti, Andrew Ruggiero

University of Cassino and Southern Lazio, Cassino I-03043, Italy

ARTICLE INFO

Keywords:
Laser powder bed fusion
Nonlinear transient thermal analysis
Temperature field
Melt pool
AlSi10Mg

ABSTRACT

Additive manufactured parts are subjected to intense thermal gradients and high temperature peaks which affect mechanical properties. Such thermal cycles can cause distortions, residual stresses and microstructural heterogeneities. Since the experimental measurement of the temperature field is extremely difficult, numerical simulation can be used to obtain a description of the phenomenon. Here, a three-dimensional computational model for the prediction of the temperature field during the laser powder bed fusion process on AlSi10Mg alloy was developed. Scan path, the geometry of the heat source and the progressive generation of the part during the process have been simulated with finite element method. This approach was used in a small scale representation, as the extremely fast temperature gradients, high scanning speeds and amount of thermal energy input make the phenomenon extremely localized. The predicted melt pool size, compared with microstructural analysis results on reference samples, was used to validate the computational model.

1. Introduction

Nowadays, the production of near-net-shape metal components via Additive Manufacturing (AM) techniques is gaining increasing attention from both industrial sectors and researchers due to high design versatility [1]. However, the quality of additively manufactured parts is not always up to the industrial standards defined for traditional manufacturing methods. One of the main challenges for AM acceptability is the definition of rigorous certification methodologies balanced with the unique demands and features of AM [2]. The definition of predictive tools and standardized testing protocols is fundamental to ensure process reliability and reproducibility [3]. From this point of view, a detailed description of the several phenomena occurring during the manufacturing process is the key to understanding the linkage between the process and the microstructural features or the overall mechanical response of printed parts. The complex heat input dynamics causes local thermal histories characterized by severe gradients and cooling rates which are responsible for residual stresses and strains, defect formation mechanisms and of different microstructural morphologies. Thus, the part quality is strictly connected to the temperature field, which is the result of the process features and its parameters [2,4] *In situ* measurements of the thermal profile are quite challenging due to the high spatial and temporal resolution required [4]. Contact sensors (thermocouples) [5,6] were used to monitor the temperature change of substrate points during the deposition. Although they have high accuracy and they are easy to calibrate, their major weakness is the inability to describe the thermal field along the energy input source path. Contactless measurements with pyrometers or thermal image cameras are more suitable for AM process monitoring since they can provide information about the area with the highest thermal dynamics. Nevertheless, multiple phenomena overlap during deposition, such as partial absorption and reflection of laser power, phase changes, evaporation, material expulsion and Marangoni flow may cause a local variation of the optical properties of the surface that is quite difficult to evaluate [7]. These technologies require an accurate estimation of the surface emissivity and the chamber transmissivity [8]. Researchers have proposed several techniques to correctly evaluate these parameters making the experimental set-up particularly complex [9], as highlighted by Yan et al. [4]. To overcome these limits, there has been a continuous effort in the development of numerical models aimed to simulate AM processes and to obtain information about the thermal field. Li et al. investigated the relationship between process parameters, the thermal profile (peak temperature, molten pool lifetime) and defects formation during a selective laser melting process of commercially pure Ti powders, comparing the numerical results with experimental microstructural analysis [10]. Wei et al. [11] proposed a 3D FEA model to evaluate the

---

[*] Corresponding author.
E-mail address: sara.ricci@unicas.it (S. Ricci).

https://doi.org/10.1016/j.finmec.2022.100109
Received 2 July 2022; Accepted 3 July 2022

Table 1
Process Parameters.

Parameter	UoM	Value
Layer thickness	mm	0.05
Laser power	W	350
Scanning speed	mm/s	1150
Hatch distance	mm	0.17
Base temperature	°C	150
Initial powder temperature	°C	65
Recoat time	s	~2.5

influence of process parameters, such as laser power and scanning speed, on the thermodynamic behavior of the melt pool. Their results highlighted a strong Marangoni flow dependence on process parameters and that an unstable flow is responsible for defects generations within the printed material. Li et al. [12] developed a thermo-mechanical model to investigate the main features of a “point-exposure” scanning strategy and, from a multi-track simulation, they observed that the highest residual stresses appeared at the overlap of different tracks. Fergani et al. [13] implemented an analytical model in Matlab to predict both the temperature field and the residual stresses and strains maps during a selective laser melting process on 316 L alloy. They found that the maximum tensile residual stresses were along the building direction and concluded that selecting an adequate scanning path may result in an optimal residual stress profile for the component. The information on the transient temperature field has also been used to predict the grain structure, coupling the thermal analysis with Cellular automata [14] or Phase-Field method [15], or to predict the phase distribution, implementing phase evolution criteria [16,17]. Therefore, the prediction of the thermal field evolution during the deposition process has a very strong capability as it is useful to understand AM process dynamics, to predict final part key features or to optimize process parameters without extensive experimental investigations. In this study, a thermal transient computational model for the description of the thermal evolution during a laser powder bed fusion LPBF process on AlSi10Mg alloy is presented and validated. The model was developed with the commercial FEM code MSC MARC v2020. The main features of the thermal field were compared to the results of a metallographic analysis on reference samples.

2. Materials and methods

2.1. Sample fabrication and material properties

AlSi10Mg samples were produced using a SLM280 Twin machine, with two parallel IPG fiber lasers and a 280 × 280 × 365 mm^3 build envelope, in a protective Argon atmosphere. The maximum laser scanning speed is 10 m/s. The laser beam follows a raster pattern with a 67° change of orientation between consecutive layers in order to guarantee a high densification level of the final part. The metallographic analysis was carried out on vertical as-built cylindrical specimens whose dimensions are 8 mm (diameter) x 36 mm (height). Process parameters are listed in Table 1. The powder initial apparent density, measured according to ASTM-B417, is 1.52 $\mathrm{g/cm}^3$.

The accurate estimation of the thermo-physical temperature-depended properties of the selected alloy is mandatory for a thorough material modeling. Indeed, during AM process, the material undergoes a complex thermal history over a wide temperature range, multiple melting and solidification. Criales et al. [18] underlined the strong dependence of the temperature profile on material properties such as conductivity, density and specific heat. In this study, those properties were obtained from *Sente JMatPro* simulation software given the initial powder chemical composition, estimated according to ASTM E1479. The effect of the latent heat was modeled through a significative discontinuity of the specific heat. The powder bed conductivity might be two times lower than the bulk material. It depends on the powder porosity, on the size and distribution of the particles, and the gas filling the voids. The powder conductivity was estimated with a semi-empirical model [19]:

$$k_p = \frac{k_s(1-\varepsilon)}{1+\psi\left(\frac{k_s}{k_p}\right)} \tag{1}$$

where k_p,$k_s$and $k_g$are powder, bulk material, and gas conductivity, ψ is an empirical coefficient and $\varepsilon$is the porosity:

$$\varepsilon = \frac{\rho_s - \rho_p}{\rho_s} \tag{2}$$

ρ_s and ρ_p are the powder and solid density.

2.2. Heat transfer in LPBF

The distribution of the temperature T in a 3D cartesian domain satisfies the following equation,

$$\rho c_p \frac{\partial T}{\partial t} = \frac{\partial}{\partial x}\left(k(T)\frac{\partial T}{\partial x}\right) + \frac{\partial}{\partial y}\left(k(T)\frac{\partial T}{\partial y}\right) + \frac{\partial}{\partial z}\left(k(T)\frac{\partial T}{\partial z}\right) + Q \tag{3}$$

In which ρ,c_p and k are the material density, specific heat and conductivity and Q is the volumetric heat input. The initial temperature distribution is espressed as,

$$T(x,y,z) = T_0, t = 0 \tag{4}$$

Where T_0 is the initial powder temperature of 65 °C. During the deposition, the laser beam travels upon the powder bed, melting the underlying layer and allowing the formation of a metallurgical bond with the already deposited tracks. At the same time, heat transfer mechanisms such as conduction, convection and radiation play a crucial role on the surface, according to:

$$k\frac{\partial T}{\partial n} = q - q_{conv} - q_{rad} \tag{5}$$

$q$is the heat input flux. The heat dissipated by conduction is much higher than the one dissipated by convection, q_{conv}, and radiation, q_{rad} [20]. Due to the small scale of this phenomenon and the very high temperature gradients, conduction with the powder bed and the underlying layer is dominant [21,22]. To decrease the computational complexity of the analysis, the heat loss through the powder bed was modeled by an equivalent convective flux, according Li et al. [23]. The heat loss to the Argon environment was neglected. Radiative heat transfer is more effective than convection within the melt pool but still less than conduction [21,22]. Thus, a constant value of 0.4 [7,17] was chosen for the material’s emissivity. The amount of laser energy absorbed by the material is difficult to evaluate given its high dependence on material thermo-physical properties, surface roughness, beam wavelength, and laser distance and orientation from the surface. The choice of a constat absorbivity coefficient has been widely used in letterature [10,11,25,26]. In this work, an absorptivity coefficient of 0.3 was selected after an inverse calibration process aimed to reduce the error between the experimental and the predicted melt pool size, as estimated in [24].

2.3. Computational model

The multiphysics phenomena that occur during the process have led researches to carry out modeling assumptions and semplifications in order to obtain a trade off between an accurate solution and the model complexity. Surely, one of the main problem in AM process simulation is the extensive computational time required to represent accurately the heat input phenomenon and its extremely rapid kinetics. As highlighted by Liu et al. [27], the temporal and spatial discretization should be detailed enough to ensure a continuous laser movement in the numerical simulation. To obtain information about the thermal field evolution at a

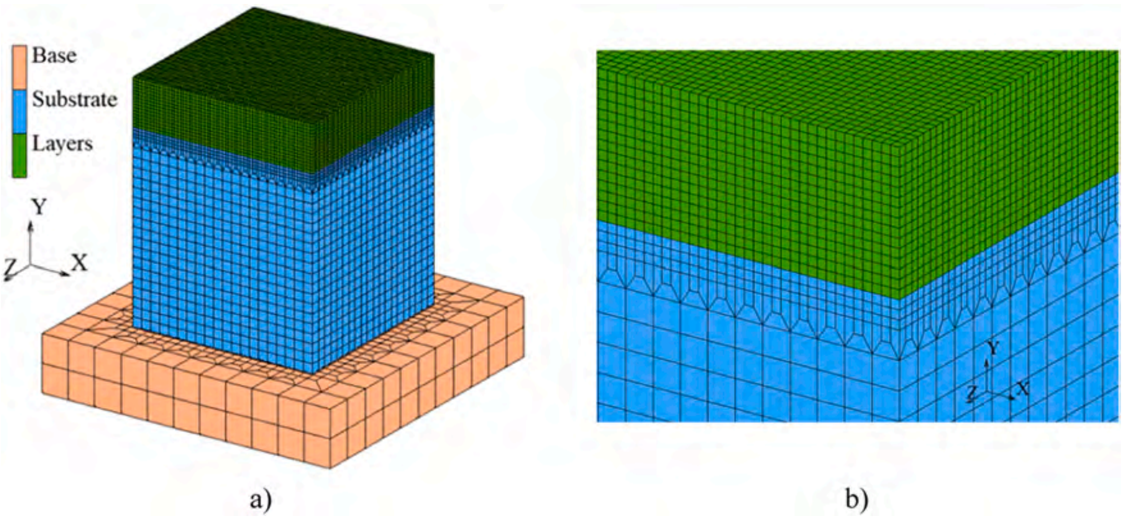

Fig. 1. Numerical model and computational grid.

part-scale level, the scale gap between the part dimension and laser spot size and the discrepancy between the time step required and the whole part generation time would made the analysis time prohibitive. This awareness led to the development of accurate simulation strategies to reduce the computational cost without losing accuracy for part-scale models. For instance, Ghanbari et al. [28] have subdivided the calculus domain in two scales, local and global. A small adaptive-local model with a very fine spatial and temporal discretization solved the thermal field around the laser heat input, while a global simulation with larger grid size and time step calculated the temperature evolution far from the area with the highest kinetics. The two temperature profiles were then combined together. Liu et al. [27] developed and implemented in a FEM code a characteristic time-based heat input (CTI) model in which the energy input phase was simulated in two numerical steps. The scanning time of a track is divided in a heating time, in which an integrated energy input is applied, and a cooling phase without energy input. Other

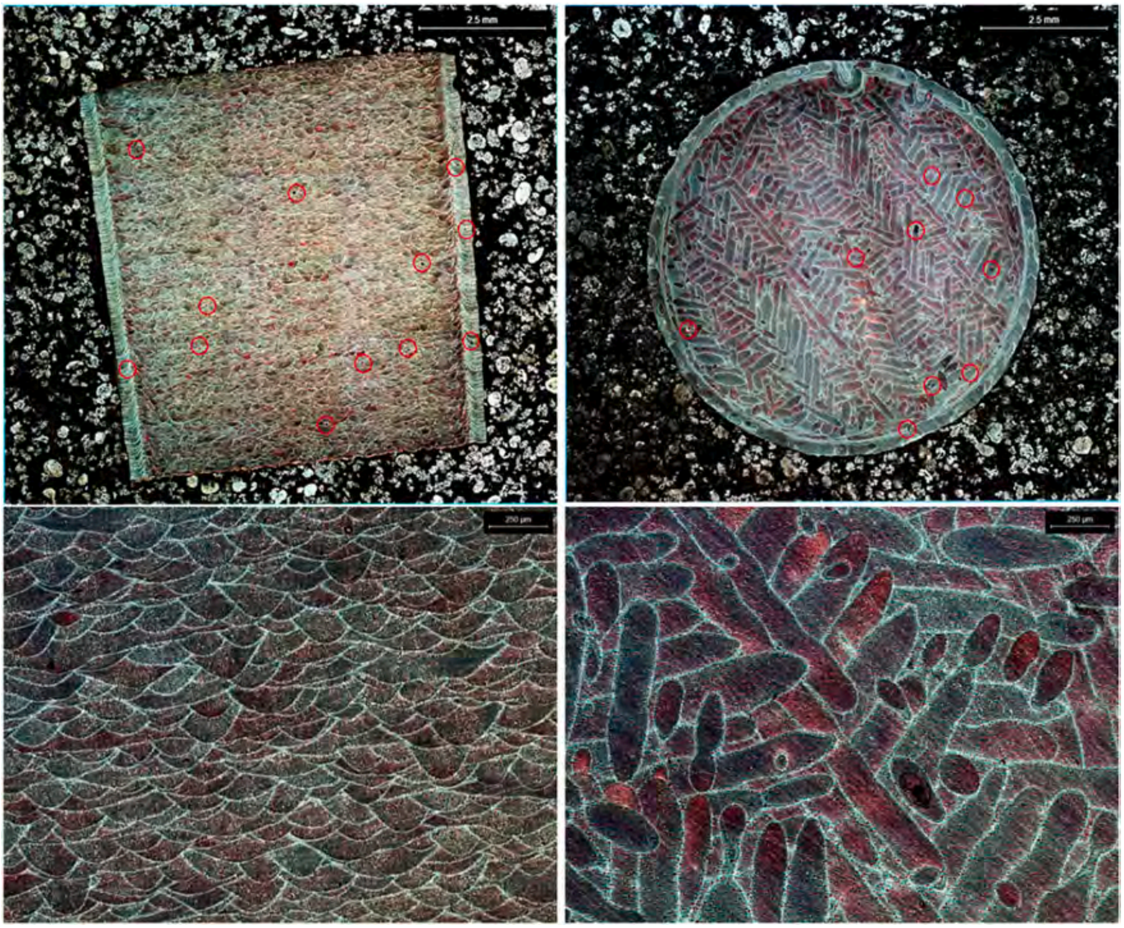

Fig. 2. Optical microscopy images - cross-section (left) top view (right) at different magnification levels.

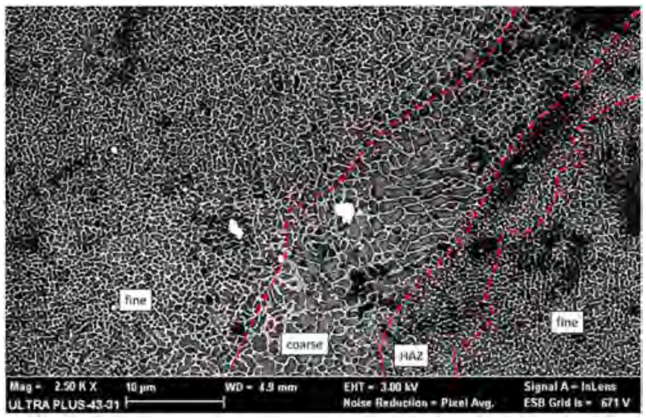

Fig. 3. SEM image shows the typical cellular microstructure of the melt pool cross-section.

authors [29–31] proposed a superposition-based semi-analytical model in which an analytical solution for point sources in a semi-infinite space is combined with numerical fields to impose boundary conditions. At the same time, the thorough description of the melt pool behavior and of the various phenomena that occur at the melt pool level requires quite accurate models that closely follow the movement of the laser input source [32]. Indeed, meso-scale model have been widely used in literature to describe local phenomena at the melt pool level to investigate key microstructural features [14,26,33] or the influence of process parameters on the thermal behavior or on defect formation mechanism [10,11,25]. This study is aimed to correlate the microstructural evidence to the thermal evolution the material undergoes during deposition, thus a meso-scale approach was chosen. Fig. 1 illustrates the computational grid, composed of hexahedral elements, with 8 integration points. The powder bed base is 1.6 × 1.6 × 0.3 mm^3, with a grid size of 0.15 × 0.15 × 0.15 mm^3. The specimen is modeled with a 1 × 1 × 1.25 mm^3 block, with a finer mesh of 0.016 × 0.016 × 0.016 mm^3 in the deposited layers. A coarser grid of 0.05 × 0.05 × 0.05 mm^3 was adopted far from the laser scan area. A glue contact was selected to replicate the welding link formed in LPBF process between the base and the part. The time step was chosen to guarantee a continuous laser motion upon the powder bed during deposition, so a constant value of 1.5×10^{-5} s was selected. During the recoat time, the time step gradually increases to a maximum of 0.15 s. The experimental parameters reported in Table 1 were used in the simulation.

The powder bed was modeled as a homogeneous mean [10,25] with scaled-down thermo-physical properties and only a thermal analysis was conducted [10,12,33], neglecting the melt pool fluidity due to its limited size [25]. To describe the change of conductivity between powder and solid, a hybrid quite-inactive element method was used. At the beginning of the analysis, all layers were inactive and not included in the calculus. Upon activation, the elements were in a quiet state, with a scaled-down conductivity, until they were crossed by the laser beam. The complex heat adduction phenomenon was simulated by a spatially variable thermal flux along a user-defined path. In literature, various solutions have been employed to model the laser beam, such as the Gaussian heat source [11,28], Goldak's double ellipsoid [27,34], or a cylindrical geometry [35], while some authors proposed their own heat source models [36,37]. In this study, the laser input source was modeled using the weld flux tool with a cylindrical-shaped geometry, which allows a more focused heat input and more penetration in the material than Goldak's ellipsoid. The radius of the cylinder is the same of the laser beam input.

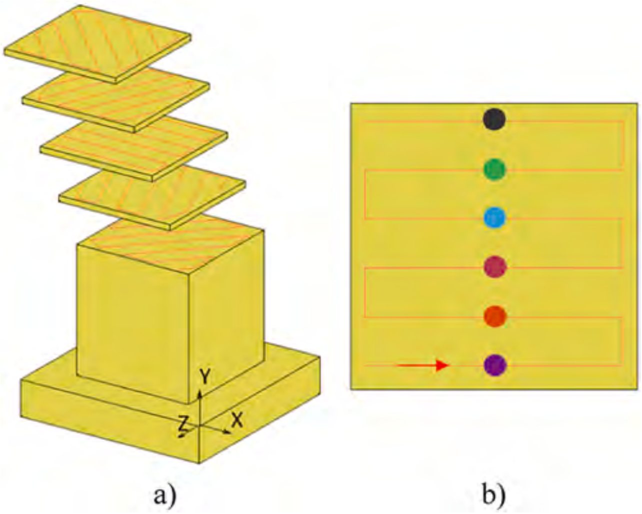

Fig. 4. (a) Scanning path and (b) measure points for the third layer.

3. Risults and discussion

3.1. Sample characterization

As-built LPBF AlSi10Mg macro- and microstructural features are strongly dependent on the manufacturing process [38]. Given the high anisotropy of AM parts, vertical section and cross-section surfaces were extracted and analyzed. All resin-embedded samples were polished and etched by Keller's reagent. The microstructural features were observed using *LEICA DM* 6000 M optical microscopy (OM) and *ZEISS ultra plus* scanning electron microscopy (SEM). The optical microscopy images, presented in Fig. 2, highlight a strong texturization of the metallic matrix, related to the layer-by-layer nature of LPBF. Indeed, the vertical plane shows the typical semicircular morphology of the overlapped melt pools and in the cross-section plane, the laser scan tracks are identifiable. To estimate the melt pool size, these images were analyzed by *ImageJ* software; the melt pool depth was determined to be 110±20 µm and the width 220±30 µm. The macrostructure along the cross-section and vertical planes is not uniform due to a 67° rotation of the scanning path for consecutive layers. As shown in Fig. 3, the major microstructural heterogeneities were found within the melt. The core of the melt pool exhibits a fine cellular structure of the α-Al phase surrounded by a continuous network of eutectic Al-Si precipitates. The cell size becomes coarser near the melt pool borders due to a change of solidification parameters [39]. Similarly to welding processes, outside the melt pool profile, there is a Heat Affected Zone (HAZ) in which Si phase coarsening causes a local rapture of the eutectic network.

3.2. Single-Layer analysis

A multi-track, multi-layer simulation was performed and the results were compared to the microstructural evidences. Fig. 4a illustrates the five reference layers with their corresponding scanning path. Firstly, the temperature evolution developed during the deposition of the 3rd layer (Fig. 4b) was investigated.

Fig. 5 illustrates the transient temperature distribution at different positions of the laser beam input. During the deposition of the first track (Fig. 5a), the influence of the heat input is localized mainly in the scanned area, in which the temperature increase is significant. On the contrary, the temperature of the remaining part of the powder bed is still close to the initial temperature of 65 °C. Due to the discontinuity of thermal conductivity between the powder and the bulk material, the heat transmission by conduction towards the powder is slower than the laser movement. In fact, the front isotherms, that face the unscanned

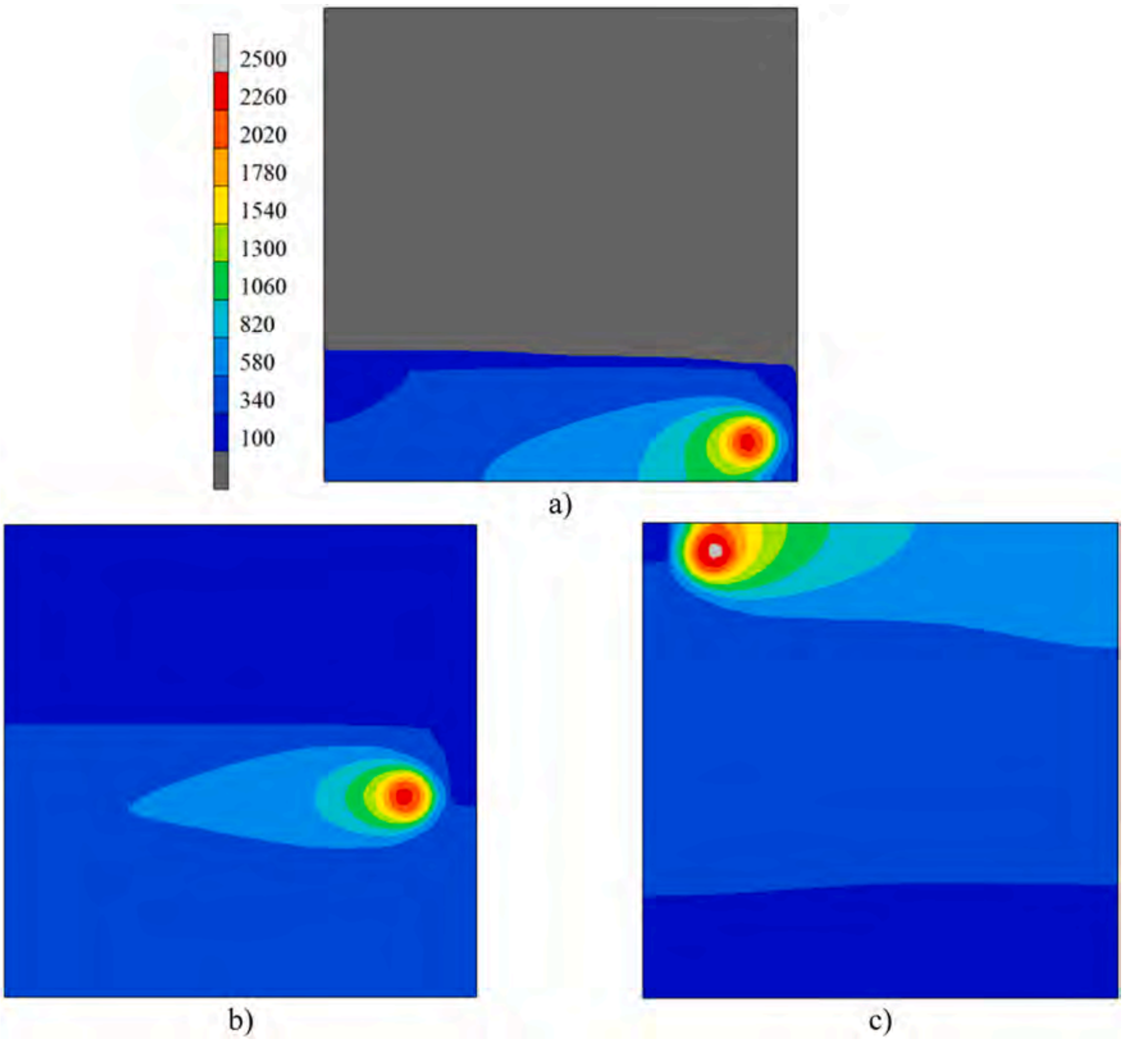

Fig. 5. Top view of the temperature distribution during the deposition of the third layer (a) end of 1st track (time 0.73 ms) (b) end of 3rd track (time 2.52 ms) (c) end of 6th track (time 5.31 ms).

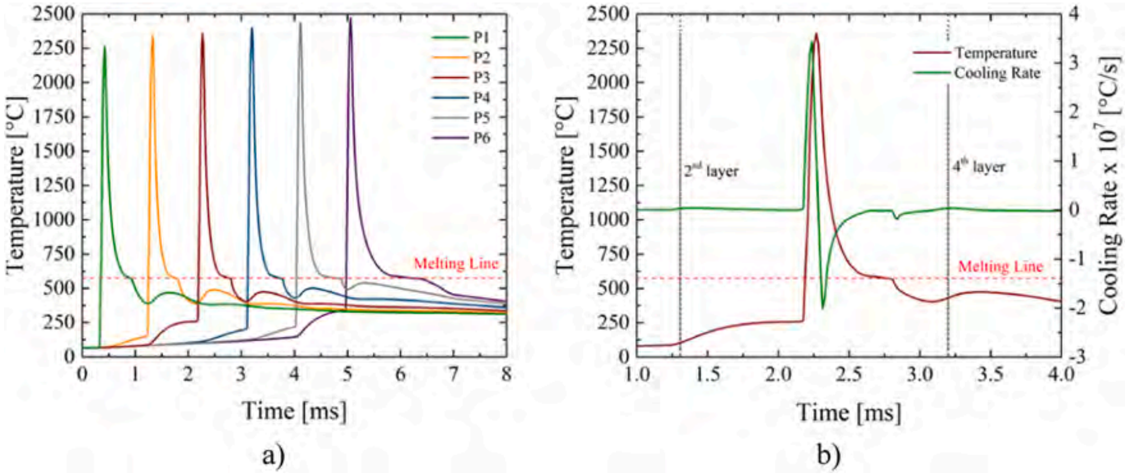

Fig. 6. a) Temperature evolution at the center of consecutive scanning tracks, b) temperature profile and the cooling rate at the center of the third scanning track.

zone, are denser than those at the back of the laser path where the material is in a solid-state state. Even during the deposition of the third track (Fig. 5b), the thermal distribution around the laser beam exhibits an asymmetrical behavior, but the powder bed temperature starts to increase because of the longer interaction time with the laser beam. This process of heat accumulation starts to decrease during the deposition of the last track (Fig. 5c), where the material starts to cool down.

The thermal evolution of the center of each track, presented in

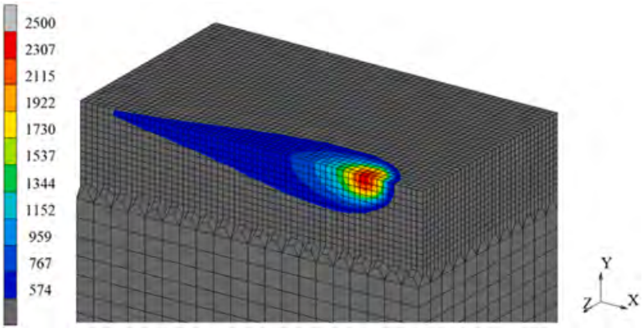

Fig. 7. Cross section view of the numerical temperature profile of the melt pool.

Fig. 6a, is characterized by very high cooling rates and temperature peaks, which far exceed AlSi10Mg melting temperature (574 °C). These results are in good agreement with the results obtained by Du et al. [25] for similar process parameters on the same alloy. The temperature peaks increase gradually from the first track to the last one, due to the heat accumulation during the deposition in the material. The influence between subsequent tracks can be clearly seen. For instance, the temperature at the center of the third track starts to gradually increase during the deposition of the second track. A content temperature increase during the deposition of the fourth track is also appreciable. A detail of the temperature change and cooling rate for the center point of the 3rd track is illustrated in Fig. 6b. An accurate description of the cooling profile and the phase change between liquidus and solidus temperatures is obtained taking into account both latent heat and material properties' temperature-dependence. For this temperature profile, the numerical cooling rate between the liquidus and solidus temperatures is 2.45×10^5 s^{-1}, which is accountable for the very fine cellular structure observed in SEM images.

3.3. Melt pool analysis and model validation

In Fig. 7, a detail of the numerical melt pool profile during the laser motion is presented. The predicted melt pool dimensions were measured at the maximum extension of the thermal profile and they were estimated, as shown in Fig. 8, with the intersection of the temperature profile and the melting line. The results are in good agreement with the experimental data presented with their corresponding uncertainty in Fig. 9. The error in the prediction of both the melt pool width and depth is less than 2%.

The thermal histories within the melt pool were extracted in the five measure points illustrated in Fig. 10.

The temperature profiles change meaningfully between the melt pool core and periphery. The latter has a more controlled thermal evolution, with lower peaks and slower cooling rates, Fig. 11, either along the width and the depth. This is in agreement with the grain size heterogeneity presented in the metallographic analysis, Fig. 3. The cell dimension is strongly dependent on the cooling rates. Along the width, the point at the periphery (W3) undergoes re-melting during the deposition of the second and the third track, as it can be clearly seen in

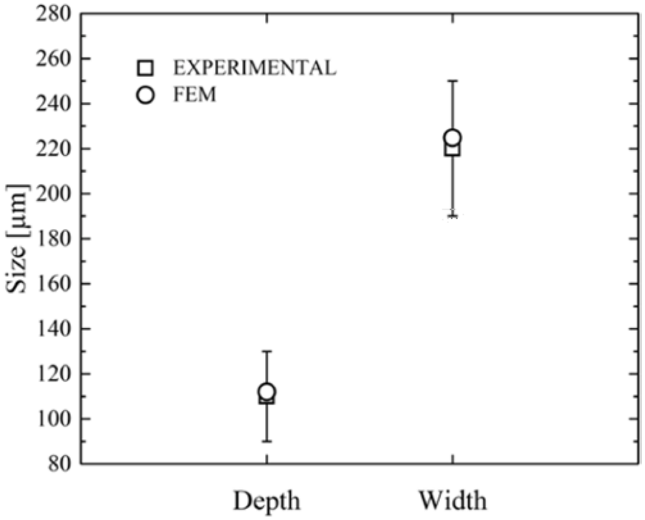

Fig. 9. Comparison of experimental and predicted melt pool size.

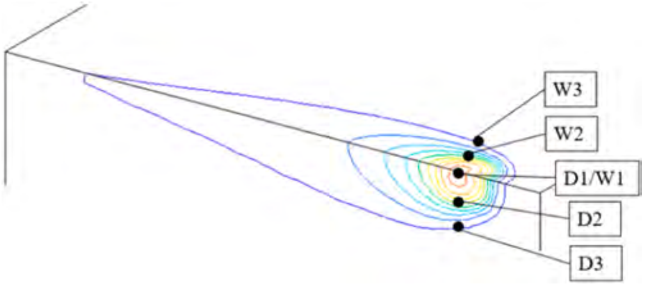

Fig. 10. Measure points within the melt pool.

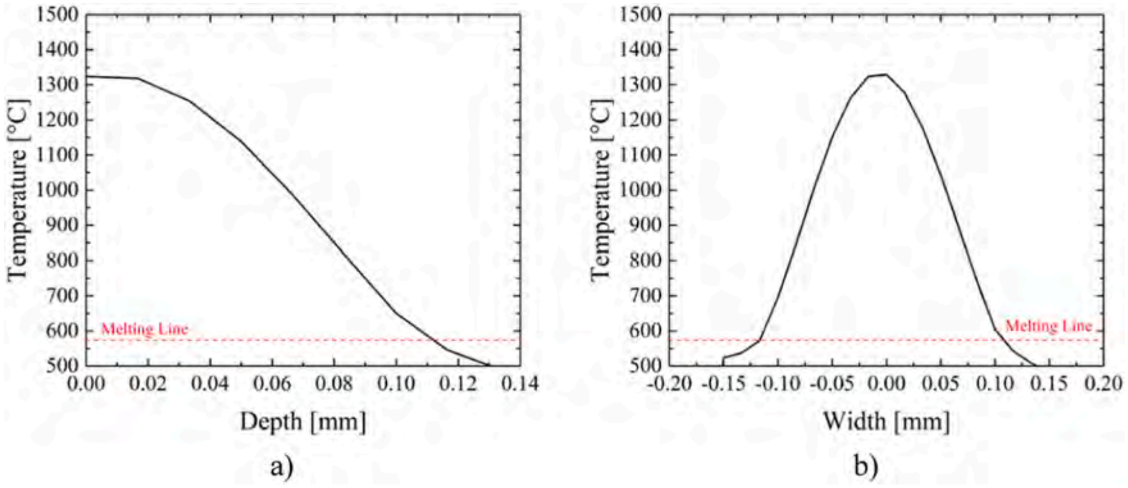

Fig. 8. Thermal profile extracted (a) along the depth (b) along the width of the melt pool.

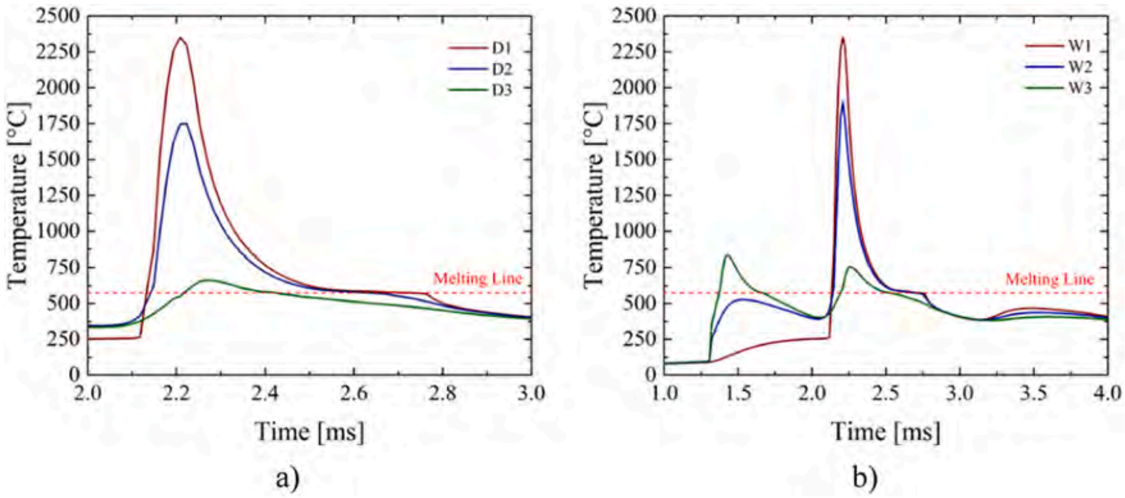

Fig. 11. Temperature distribution profiles within the melt pool (a) depth and (b) width.

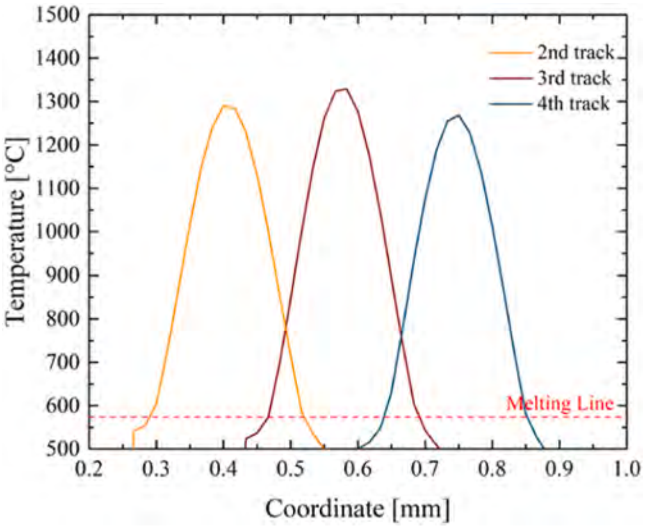

Fig. 12. Overlap of temperature profiles for subsequent tracks.

Fig. 11b. Indeed, the measured melt pool width is greater than the hatch spacing (0.17 mm), and this condition must be satisfied in order to guarantee a high densification level and reduce voids formation after the scans. The overlap of the temperature profiles for three consecutive tracks is shown in Fig. 12. The melt pool width increases slightly during the deposition for the heat accumulation phenomenon. The predicted melt pool width is 213.4, 224.8 and 229.5 μm during the deposition of the second, third and fourth track respectively.

3.4. Multi-layer analysis

During a LPBF process, the material undergoes a complex thermal cycle, with repeated melting and solidification. The deposition of a new layer requires an additional energy input that has a variable thermal influence on the solidified layers. Figs. 13 and14 show the thermal cycle measured at the center point of the first and second layers. Each layer undergoes severe re-melting during the deposition of the subsequent one: this condition guarantees the formation of a metallurgical bond between the two. The experimental melt pool size is a little greater than the sum of two layers thickness. Since the phenomenon is extremely localized, the thermal influence on other layers is limited, as supported by the numerical results. Fig. 15 underlines a self-similarity between the thermal histories of corresponding points of different layers. This result is corroborated by the experimental evidence since no microstructural gradients were found along the building direction.

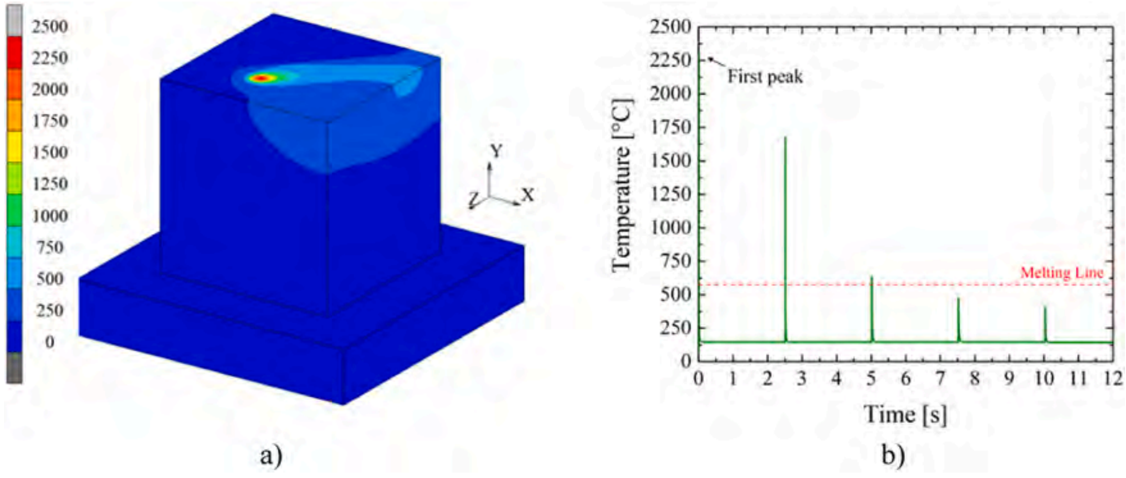

Fig. 13. Temperature map and thermal cycle evolution for the point at the middle of the 1st layer.

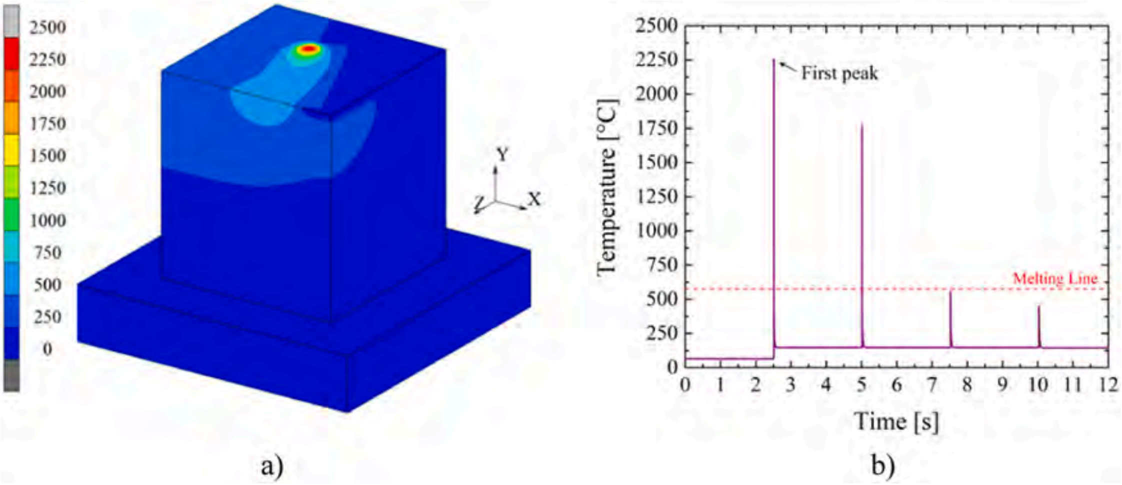

Fig. 14. Temperature map and thermal cycle evolution for the point at the middle of the 2nd layer.

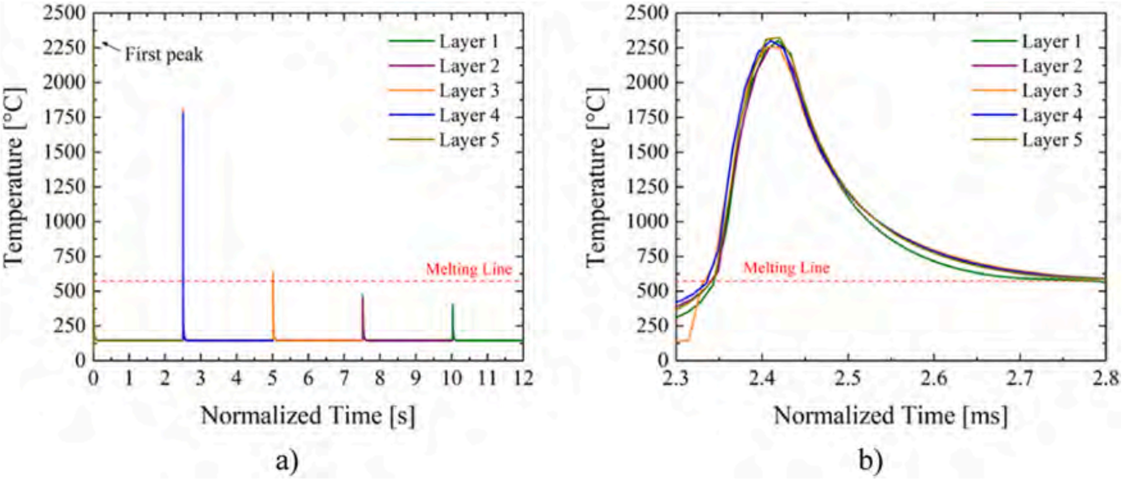

Fig. 15. Temperature cycle of different layers, (a) normalized thermal histories, (b) detail.

4. Conclusions

In this work, a 3D transient computational model was developed in the commercial FEM code MSC Marc to investigate the temperature field evolution during a LPBF process on AlSi10Mg alloy. The numerical results of a multi-track and multi-layer simulation were discussed regarding the experimental evidence. To validate the computational model, the predicted melt pool size was compared to the experimental one, and the results were satisfactory, with an error in the prediction of both the width and the depth less than 2%. OM and SEM analysis underlined a strong dependence of AlSi10Mg microstructure on the manufacturing process. The macrostructure shows a distinctive layered texture with overlapping melt pool profiles that represent the scanning path followed by the laser heat input. The major microstructural heterogeneities were found within the melt pool profile, with a variable cell size between the core and the periphery. Those features were linked to the thermal evolutions predicted by the model. Indeed, the temperature profiles of different points in a multi-track or a multi-layer analysis were comparable. Meanwhile, dissimilar thermal evolutions were experienced at different points of the melt pool, where the major thermal gradients can be found.

Declaration of Competing Interest

The authors declare that they have no known competing financial interests or personal relationships that could have appeared to influence the work reported in this paper.

Acknowledgments

This work was funded by the Italian Ministry of defence under Grant No. PNRM/a2017.079. The experimental activity was carried out with *BeamIt Spa,* a leading supplier company for additively manufactured parts, which provided information about the LPBF process and the reference samples, and with the Italian Air Force - *D.A.S.A.S.* (Divisione Aerea di Sperimentazione Aeronautica e Spaziale), which performed the metallographic analysis.

References

[1] S.A.M. Tofail, E.P. Koumoulos, A. Bandyopadhyay, S. Bose, L. O'Donoghue, C. Charitidis, Additive manufacturing: scientific and technological challenges, market uptake and opportunities, Mater. Today 21 (2018) 22–37, https://doi.org/10.1016/j.mattod.2017.07.001.
[2] R.M. Taylor, J. Manzo, L. Flansburg, Certification strategy for additively manufactured structural fittings, Solid Free. Fabr, in: 2016 Proc. 27th Annu. Int. Solid Free. Fabr. Symp. - An Addit. Manuf. Conf. SFF 2016, 2016, pp. 1985–2000.

[3] R.A. Bae Chang-Jun, Diggs Alisha, Quantification and Certification of Additive Manufacturing Materials and Processes, Elsevier Inc., 2016, https://doi.org/10.1007/978-3-319-23362-8.

[4] Z. Yan, W. Liu, Z. Tang, X. Liu, N. Zhang, M. Li, H. Zhang, Review on thermal analysis in laser-based additive manufacturing, Opt. Laser Technol. 106 (2018) 427–441, https://doi.org/10.1016/j.optlastec.2018.04.034.

[5] E.R. Denlinger, V. Jagdale, G.V. Srinivasan, T. El-Wardany, P. Michaleris, Thermal modeling of Inconel 718 processed with powder bed fusion and experimental validation using in situ measurements, Addit. Manuf. 11 (2016) 7–15, https://doi.org/10.1016/j.addma.2016.03.003.

[6] C. S, O. Akyildiz, D. Candemir, Q. Yang, A.C. To, Predicting microstructure evolution during D1irected energy deposition additive manufacturing of Ti-6Al-4V, J. Manuf. Sci. Eng. Trans. ASME. 140 (2018) 1–11, https://doi.org/10.1115/1.4038894.

[7] N. Schnell, M. Schoeler, G. Witt, S. Kleszczynski, Experimental and numerical thermal analysis of the laser powder bed fusion process using in situ temperature measurements of geometric primitives, Mater. Des. 209 (2021), 109946, https://doi.org/10.1016/j.matdes.2021.109946.

[8] C.G. Ren, Y.L. Lo, H.C. Tran, M.H. Lee, Emissivity calibration method for pyrometer measurement of melting pool temperature in selective laser melting of stainless steel 316L, Int. J. Adv. Manuf. Technol. 105 (2019) 637–649, https://doi.org/10.1007/s00170-019-04193-0.

[9] R.D. Murphy, E.C. Forrest, A review of In-situ temperature measurements for additive manufacturing technologies, in: 2016 NCSL Int. Work. Symp, 2016.

[10] Y. Li, D. Gu, Thermal behavior during selective laser melting of commercially pure titanium powder: numerical simulation and experimental study, Addit. Manuf. 1 (2014) 99–109, https://doi.org/10.1016/j.addma.2014.09.001.

[11] W. Pei, W. Zhengying, C. Zhen, L. Junfeng, Z. Shuzhe, D. Jun, Numerical simulation and parametric analysis of selective laser melting process of AlSi10Mg powder, Appl. Phys. A Mater. Sci. Process. 123 (2017) 1–15, https://doi.org/10.1007/s00339-017-1143-7.

[12] Z. Li, S. Yang, B. Liu, W. Liu, Z. Kuai, Y. Nie, Simulation of temperature field and stress field of selective laser melting of multi-layer metal powder, Opt. Laser Technol. 140 (2021), 106782, https://doi.org/10.1016/j.optlastec.2020.106782.

[13] O. Fergani, F. Berto, T. Welo, S.Y. Liang, Analytical modelling of residual stress in additive manufacturing, Fatigue Fract. Eng. Mater. Struct. 40 (2017) 971–978, https://doi.org/10.1111/ffe.12560.

[14] O. Zinovieva, A. Zinoviev, V. Ploshikhin, Three-dimensional modeling of the microstructure evolution during metal additive manufacturing, Comput. Mater. Sci. 141 (2018) 207–220, https://doi.org/10.1016/j.commatsci.2017.09.018.

[15] C. Kumara, Microstructure modelling of additive manufacturing of alloy 718, 2018.

[16] J. Irwin, E.W. Reutzel, P. Michaleris, J. Keist, A.R. Nassar, Predicting microstructure from thermal history during additive manufacturing for Ti-6Al-4V, J. Manuf. Sci. Eng. Trans. ASME. 138 (2016) 1–11, https://doi.org/10.1115/1.4033525.

[17] E. Salsi, M. Chiumenti, M. Cervera, Modeling of microstructure evolution of Ti6Al4V for additive manufacturing, Metals (Basel) 8 (2018), https://doi.org/10.3390/met8080633.

[18] L.E. Criales, Y.M. Arısoy, T. Özel, Sensitivity analysis of material and process parameters in finite element modeling of selective laser melting of Inconel 625, Int. J. Adv. Manuf. Technol. 86 (2016) 2653–2666, https://doi.org/10.1007/s00170-015-8329-y.

[19] J. Xing, W. Sun, R.S. Rana, 3D modeling and testing of transient temperature in selective laser sintering (SLS) process, Optik (Stuttg) 124 (2013) 301–304, https://doi.org/10.1016/j.ijleo.2011.11.064.

[20] Y. Li, D. Gu, Parametric analysis of thermal behavior during selective laser melting additive manufacturing of aluminum alloy powder, Mater. Des. 63 (2014) 856–867, https://doi.org/10.1016/j.matdes.2014.07.006.

[21] Z. Luo, Y. Zhao, A survey of finite element analysis of temperature and thermal stress fields in powder bed fusion Additive Manufacturing, Addit. Manuf. 21 (2018) 318–332, https://doi.org/10.1016/j.addma.2018.03.022.

[22] B. Schoinochoritis, D. Chantzis, K. Salonitis, Simulation of metallic powder bed additive manufacturing processes with the finite element method: a critical review, Proc. Inst. Mech. Eng. Part B J. Eng. Manuf. 231 (2017) 96–117, https://doi.org/10.1177/0954405414567522.

[23] C. Li, M.F. Gouge, E.R. Denlinger, J.E. Irwin, P. Michaleris, Estimation of part-to-powder heat losses as surface convection in laser powder bed fusion, Addit. Manuf. 26 (2019) 258–269, https://doi.org/10.1016/j.addma.2019.02.006.

[24] J. Ning, D.E. Sievers, H. Garmestani, S.Y. Liang, Analytical thermal modeling of metal additive manufacturing by heat sink solution, Materials (Basel) 12 (2019) 1–15, https://doi.org/10.3390/ma12162568.

[25] Y. Du, X. You, F. Qiao, L. Guo, Z. Liu, A model for predicting the temperature field during selective laser melting, Results Phys. 12 (2019) 52–60, https://doi.org/10.1016/j.rinp.2018.11.031.

[26] Y.S. Lee, W. Zhang, Modeling of heat transfer, fluid flow and solidification microstructure of nickel-base superalloy fabricated by laser powder bed fusion, Addit. Manuf. 12 (2016) 178–188, https://doi.org/10.1016/j.addma.2016.05.003.

[27] M. Liu, L.N.S. Chiu, C. Vundru, Y. Liu, A. Huang, C. Davies, X. Wu, W. Yan, A characteristic time-based heat input model for simulating selective laser melting, Addit. Manuf. 44 (2021), 102026, https://doi.org/10.1016/j.addma.2021.102026.

[28] P. Gh Ghanbari, E. Mazza, E. Hosseini, Adaptive local-global multiscale approach for thermal simulation of the selective laser melting process, Addit. Manuf. 36 (2020), 101518, https://doi.org/10.1016/j.addma.2020.101518.

[29] Y. Yang, F. van Keulen, C. Ayas, A computationally efficient thermal model for selective laser melting, Addit. Manuf. 31 (2020), 100955, https://doi.org/10.1016/j.addma.2019.100955.

[30] Y. Yang, M.F. Knol, F. van Keulen, C. Ayas, A semi-analytical thermal modelling approach for selective laser melting, Addit. Manuf. 21 (2018) 284–297, https://doi.org/10.1016/j.addma.2018.03.002.

[31] T.P. Moran, D.H. Warner, N. Phan, Scan-by-scan part-scale thermal modelling for defect prediction in metal additive manufacturing, Addit. Manuf. 37 (2021), 101667, https://doi.org/10.1016/j.addma.2020.101667.

[32] M. Bayat, W. Dong, J. Thorborg, A.C. To, J.H. Hattel, A review of multi-scale and multi-physics simulations of metal additive manufacturing processes with focus on modeling strategies, Addit. Manuf. 47 (2021), 102278, https://doi.org/10.1016/j.addma.2021.102278.

[33] T.N. Le, Y.L. Lo, Z.H. Lin, Numerical simulation and experimental validation of melting and solidification process in selective laser melting of IN718 alloy, Addit. Manuf. 36 (2020), 101519, https://doi.org/10.1016/j.addma.2020.101519.

[34] L. Parry, I.A. Ashcroft, R.D. Wildman, Understanding the effect of laser scan strategy on residual stress in selective laser melting through thermo-mechanical simulation, Addit. Manuf. 12 (2016) 1–15, https://doi.org/10.1016/j.addma.2016.05.014.

[35] A. Foroozmehr, M. Badrossamay, E. Foroozmehr, S. Golabi, Finite element simulation of selective laser melting process considering optical penetration depth of laser in powder bed, Mater. Des. 89 (2016) 255–263, https://doi.org/10.1016/j.matdes.2015.10.002.

[36] E.J. Schwalbach, S.P. Donegan, M.G. Chapman, K.J. Chaput, M.A. Groeber, A discrete source model of powder bed fusion additive manufacturing thermal history, Addit. Manuf. 25 (2019) 485–498, https://doi.org/10.1016/j.addma.2018.12.004.

[37] K.H. Lee, G.J. Yun, A novel heat source model for analysis of melt Pool evolution in selective laser melting process, Addit. Manuf. 36 (2020), 101497, https://doi.org/10.1016/j.addma.2020.101497.

[38] P. Wei, Z. Wei, Z. Chen, J. Du, Y. He, J. Li, Y. Zhou, The AlSi10Mg samples produced by selective laser melting: single track, densification, microstructure and mechanical behavior, Appl. Surf. Sci. 408 (2017) 38–50, https://doi.org/10.1016/j.apsusc.2017.02.215.

[39] L. Thijs, K. Kempen, J.P. Kruth, J. Van Humbeeck, Fine-structured aluminium products with controllable texture by selective laser melting of pre-alloyed AlSi10Mg powder, Acta Mater. 61 (2013) 1809–1819, https://doi.org/10.1016/j.actamat.2012.11.052.